LETTER
SPACE PHYSICS: INTERPLANETARY PHYSICS

Earth and Planetary Physics
5: 218–222, 2021
doi: 10.26464/epp2021020

A new inversion method for reconstruction of plasmaspheric He^+ density from EUV images

Ya Huang[1], Lei Dai[1*], Chi Wang[1], RongLan Xu[1], and Liang Li[2]

[1]State Key Laboratory of Space Weather, National Space Science Center, Chinese Academy of Sciences, Beijing 100190, China;

[2]Department of Engineering Physics, Tsinghua University, Beijing 100084, China

Key Points:

- Present a new method to reconstruct the plasmaspheric He^+ global density distribution from two dimensional Extreme Ultraviolet images.
- The new method has superior performance with insufficient projection data.
- The method can be generalized to study soft X-ray images from the Solar wind–Magnetosphere–Ionosphere Link Explorer mission.

Citation: Huang, Y., Dai, L., Wang, C., Xu, R. L. and Li, L. (2021). A new inversion method for reconstruction of plasmaspheric He^+ density from EUV images. *Earth Planet. Phys.*, *5*(2), 218–222. http://doi.org/10.26464/epp2021020

Abstract: The Computer Tomography (CT) method is used for remote sensing the Earth's plasmasphere. One challenge for image reconstruction is insufficient projection data, mainly caused by limited projection angles. In this study, we apply the Algebraic Reconstruction Technique (ART) and the minimization of the image Total Variation (TV) method, with a combination of priori knowledge of north–south symmetry, to reconstruct plasmaspheric He^+ density from simulated EUV images. The results demonstrate that incorporating priori assumption can be particularly useful when the projection data is insufficient. This method has good performance even with a projection angle of less than 150 degrees. The method of our study is expected to have applications in the Soft X-ray Imager (SXI) reconstruction for the Solar wind–Magnetosphere–Ionosphere Link Explorer (SMILE) mission.

Keywords: Earth plasmasphere He^+ density; algebraic reconstruction technique; image total variation; north–south symmetry; SXI image reconstruction; SMILE mission

1. Introduction

The plasmasphere consists of cold and dense plasmas that encircle Earth. Although the dominant ion species (H^+) has no optical emissions, Extreme Ultraviolet (EUV) light from the 30.4-nm resonance line of He^+ (He^+/H^+ is 0.1–0.2, Craven et al., 1997) is routinely used for remote sensing the plasmasphere (Meier et al., 1998; Nakamura et al., 2000). The first fully global plasmaspheric image was captured by the EUV imager onboard the Imager for Magnetopause-to-Aurora Global Exploration (IMAGE) spacecraft launched in 2000 (Sandel et al., 2000). In 2013, the Chang'e-3 (CE-3) mission successfully obtained moon-based EUV images of the Earth's plasmasphere (Li CL et al., 2015; He H et al., 2016).

The brightness of each pixel in the two dimensional (2D) EUV image is proportional to the integrated density of He^+ along the line of sight. To obtain the three dimension (3D) global density distribution of plasmaspheric He^+, a reconstruction from 2D EUV images obtained by satellites at different positions is needed. The reconstruction process is the same as in Computed Tomography (CT). The conditions for accurate plasmaspheric reconstruction with a CT algorithm based on EUV images were shown by Li L et al. (2009). The Algebraic Reconstruction Technique (ART), a common algorithm in CT, was used to reconstruct plasmaspheric He^+ density (Huang Y et al., 2009; Jin X et al., 2011). Application of the minimization of the image Total Variation (TV), i.e., "ART-TV" method, is used to further optimize the reconstruction results (Huang Y et al., 2012, 2016).

An exact reconstruction with CT algorithms requires sufficient 2D projection data. The projection angle represents the range of angles within which the object can be clearly observed without any obstacle, and is usually limited for imaging satellites. One of the most important requirements is that the projection angle should not be less than 180 degrees for any random point of the object (Tuy, 1983; Li L et al., 2008). For instance, the projection angle of IMAGE is about 90 degrees for a single orbit. In addition, the blocking of emissions by the Earth may further reduce the projection angle.

In CT reconstruction, the addition of priori knowledge is usually applied to improve the quality of the reconstructed image and reduce the requirements for the coverage of projection data (Li CF et al., 2004). Along this line of consideration, we add the assumption of north–south symmetry for the plasma density distribution in the CT reconstruction of the Earth's plasmasphere. This as-

Correspondence to: L. Dai, ldai@spaceweather.ac.cn
Received 06 NOV 2020; Accepted 27 JAN 2021.
Accepted article online 23 FEB 2021.

sumption is reasonable from the modeling and observations of the plasmasphere (Cummings et al., 1969; Orr and Matthew, 1971; Ozhogin et al., 2012; Kim et al., 2018). In this study, we demonstrate that the ART-TV method combined with the priori assumptions which is referred as the "ART-TV-S" method, is more accurate and effective for EUV image reconstruction of the plasmasphere.

The ART-TV-S method is also expected to have applications for the upcoming SMILE (Solar wind–Magnetosphere–Ionosphere Link Explorer) mission. The SMILE spacecraft will provide a Soft X-ray Image (SXI) of the magnetosheath and the cusp region of the Earth's magnetosphere (Wang C and Branduardi-Raymond, 2018). Similar to EUV, the imaging process of SXI is also consistent with the projection process of emission CT. With an assumption of north–south symmetry of the magnetosphere, the ART-TV-S method may be more accurate and effective for producing a CT reconstruction of the Earth's magnetosphere.

2. Mathematical Model and Method

2.1 Mathematical Model

The mathematical model includes both plasmaspheric He^+ and the ionosphere, since other ions in the latter can also be detected by the EUV imager. Although there are some physically relevant models (Carpenter and Anderson, 1992; Huang XQ et al., 2004; Ozhogin et al., 2012), following the example of CT (Hsieh, 2009), the He^+ in the plasmasphere and the ionosphere is assumed to be distributed uniformly. Using a uniform distribution model can more directly test the effectiveness of the method; the detailed benefits of this are explained in Huang Y et al., 2012. The inner and outer boundary of the plasmasphere are assumed to be $1.2R_e$ and $4R_e\cos^2\varnothing$ respectively, where $\varnothing$ is latitude and R_e is the Earth's radius. The plasmasphere outer boundary intersects with the equatorial plane at $4R_e$, and the density of the ionosphere and plasmasphere are set to 10 and 1, respectively. EUV is excited by the scattering of sunlight, however, Earth blocks this solar radiation. As a result, there is a zone on the night side where no EUV radiation is emitted, which is marked as the "shadow zone" in yellow in Figure 1.

2.2 Method

Since He^+ radiation is optically thin, the column-integrated intensity I for a given line of sight $\boldsymbol{L}$ can be written as:

$$I_L = \left(p(\theta)g \times 10^{-6}/4\pi\right)\int_L n(\boldsymbol{s})\mathrm{d}\boldsymbol{s},$$

where θ is the angle between the Sun–Earth line and the scattered direction towards the camera,

$$p(\theta) = 1 + 1/4(2/3 - \sin^2\theta)$$

is the phase function, g is the emission rate for He^+, and $n(\boldsymbol{s})$ is the He^+ density at position $\boldsymbol{s}$ (He F et al., 2011). For a given scattering point, $p(\theta)$ can be calculated easily, thus the column density v along $\boldsymbol{L}$ can be written as:

$$v_L = 4\pi I_L \times 10^6/(p(\theta)g) = \int_L n(\boldsymbol{s})\,\mathrm{d}\boldsymbol{s}.$$

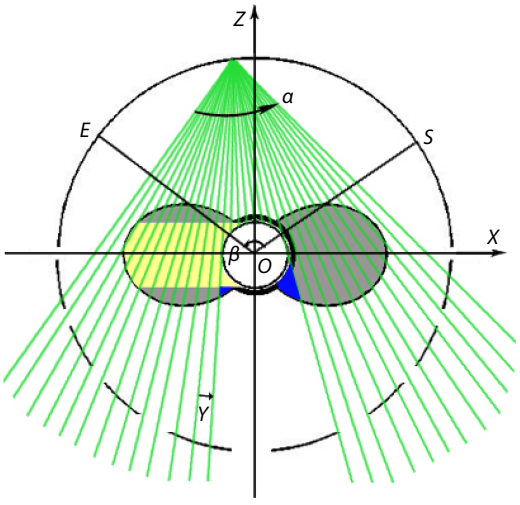

Figure 1. Illustration of circular fan-beam EUV scanning with the plasmaspheric model.

This relation is similar to CT, which allows reconstruction of the 3D density distribution of He^+ using the CT method. By combining all the column densities (also called projection data in CT) of different pixels, a set of linear integral equations can be obtained. The density n is determined by solving these equations simultaneously, however for insufficient projection data, the density n cannot be solved accurately. In this case, iterative algorithms such as ART are often recommended.

2.2.1 ART algorithm

The essence of the ART algorithm is to use an iterative method to solve a set of linear equations (Herman, 1980). If we denote j for the space position and $\boldsymbol{v}_{i,j}$ for the column density of pixel i, then the column density and the plasmaspheric He^+ density to be reconstructed are related by the equation: $\boldsymbol{v}_{i,j} = \boldsymbol{m}_{i,j}n$, where $\boldsymbol{m}_{i,j}$ represents the corresponding system matrix vector. The density n can be calculated by solving the discrete linear system of $\boldsymbol{V} = \boldsymbol{M}n$. The algorithm first assumes an initial value n^0 and then estimates n^1 by the first iteration according to n^0. The iteration continues until the termination condition is satisfied. Our implementation produces n^{k+1} from n^k by the equation:

$$n^{k+1} = n^k + \lambda^k \frac{v_i - \boldsymbol{M}_i n^k}{||\boldsymbol{M}_i||^2} \quad \text{when} \quad ||\boldsymbol{M}_i||^2 \neq 0,$$

and $n^{k+1} = n^k$ when $||\boldsymbol{M}_i||^2 = 0$,

where v_i is the measured data from the i th EUV sight, and $\boldsymbol{M}_i$ is the number i vector of the projection matrix $\boldsymbol{M}$. The relaxation parameter λ^k is used to control the convergence speed. Note that we only need to consider a single ray in each iterative step.

2.2.2 TV minimization

The CT reconstruction based on TV minimizes the image total variation under the constraint of projection equations (Sidky et al., 2006). This can be expressed as:

$$\min_{\boldsymbol{V}=\boldsymbol{M}n} ||n||_{\mathrm{TV}} \quad \text{or} \quad |\boldsymbol{M}n - \boldsymbol{V}| \leq \varepsilon,$$

where ε is tolerance parameter. The tolerance parameter is intro-

duced to relax the data fidelity constraint to accommodate inconsistencies within the measured data. For a 2D example, the TV-norm can be defined as:

$$||n||_{\mathrm{TV}} = \sum_{x,z} |\nabla n| = \sum_{x,z} \sqrt{(n_{x,z} - n_{x-1,z})^2 + (n_{x,z} - n_{x,z-1})^2}.$$

2.2.3 Plasmaspheric North–South symmetry

Since the density distribution is assumed to possess north–south symmetry, we only need to calculate the density in either the northern or southern hemisphere. In this work, we calculate the density in the northern hemisphere, and then copy the density to the southern hemisphere. Moreover, the assumption of north–south symmetry is also used in the ART step. For each single ray passing through different points ($P_{\mathrm{S}1}$, $P_{\mathrm{S}2}$, $P_{\mathrm{S}3}$,...) in the southern hemisphere, the densities of the symmetric points ($P_{\mathrm{N}1}$, $P_{\mathrm{N}2}$, $P_{\mathrm{N}3}$,...) in the northern hemisphere are corrected with the ART algorithm. This is essential for improving the reconstruction results with limited projection data.

2.2.4 Steps of reconstruction

We use n_{N} and n_{S} to denote the plasmaspheric He^+ density in the northern and southern hemisphere, respectively. The steps of the ART-TV-S method are:

(1) Initialization of the original density. In this work, the initial value n^0 is 0.

(2) Data projection iteration for n_{N} with the ART algorithm.

(3) Positivity constraint for n_{N}, and zero constraint for the shadow zone of n_{N}. The plasmaspheric density value is non-negative and treated as zero in the shadow zone.

(4) TV minimization for n_{N}.

(5) Adjustment of n_{S} based on north–south symmetry.

(6) Initialization of the next loop. The obtained density is used as the initial density for the next loop.

Repeat steps (2)–(6) until the termination condition is satisfied, or there is no appreciable change in the intermediate density after step (3). For comparison, steps (4) and (5) are omitted in the ART algorithm; step (5) is omitted for the ART-TV algorithm. Note that in each step, the complete density n which includes n_{N} and n_{S} should be calculated for both the ART and ART-TV algorithms.

3. Numerical Simulation

The numerical simulation is performed in a coordinate system with the origin at the Earth's center and the Sun–Earth line as the *X*-axis. The satellite orbit is in the *XZ* plane, and the *Z*-axis is the rotating symmetrical axis of the plasmaspheric model. The plasmaspheric shadow zone is a cylinder with its centerline on the *X*-axis. The $Y = 0$ plane as shown in Figure 1 is one of the center planes for the shadow zone, where the projection data is mostly insufficient. Such a plane is a challenge for any reconstruction algorithm, thus the 2D simulations will be performed using this plane. In Figure 1, the zone marked by the in blue is unable to be detected because Earth blocks the propagation of EUV emissions. The blue zone is thus referred to as the "undetected zone," and its position and size vary with the observation position of the satellite. Cone-beam scanning is reduced to fan-beam scanning in 2D case, and to further simplify the simulation, circular fan-beam scanning is used. The orbital shape does not affect the essence of the CT reconstruction algorithm. The exact reconstruction mainly depends on the algorithms, projection angle and sampling interval (eg., Hsieh, 2009).

3.1 Simulation Parameters

As shown in Figure 1, the diameter of the circular scanning orbit is $12R_{\mathrm{e}}$ with Earth as its center. The detector's field-of-view (fan-angle) is $\alpha = 75^{\circ}$, which is large enough to ensure the full plasmasphere is observed. The detector is modeled as a straight-line array of 150 rays per projection, so the angle γ between two neighboring rays is 0.5 degrees. The sampling trajectory is symmetrical about the *Z*-axis, with the two points *S* and *E* denoting the start and end positions of the sampling, respectively. The total angle between the two lines of *OS* and *OE* is the projection angle β. The detector is sampled at a rate of $\alpha = 1^{\circ}$. The reconstruction region is a $9R_{\mathrm{e}} \times 9R_{\mathrm{e}}$ box with $X = [-4.5R_{\mathrm{e}}, 4.5R_{\mathrm{e}}]$ and $Z = [-4.5R_{\mathrm{e}}, 4.5R_{\mathrm{e}}]$, corresponding to a 150×150 pixel array with an interval of $0.06R_{\mathrm{e}}$.

3.2 Analysis of Simulation Results

We evaluate the performance of the ART-TV and ART-TV-S methods with different projection angle β. In our simulations, β starts from 45 degrees and gradually increases to 330 degrees in steps of $\Delta\beta$ of 15 degrees. The Correlation coefficients (*Cc*) between the reconstructed results and the model are then calculated for the ART-TV and ART-TV-S methods, shown in Figure 2 using solid and dotted lines, respectively.

Figure 2 shows that the *Cc* for both methods increases with the projection angle β. In general, the reconstructed image is closer to the model with more projection data (larger projection angle β). The *Cc* ceases to increase when β is large enough, which means there is a threshold value of β; if it is beyond the threshold value, then the projection data is sufficient for the exact reconstruction. The threshold value is 150 degrees for the ART-TV-S method and 195 degrees for the ART-TV method, which illustrates that the a priori knowledge of north–south symmetry can reduce the re-

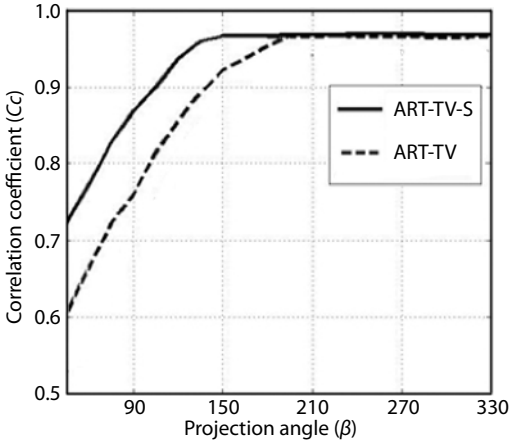

Figure 2. The correlation coefficients between the reconstructed results and the model for the ART-TV (solid line) and ART-TV-S (dotted line) methods.

quirement for projection data. Usually, projection data with $\beta = 180^\circ$ is sufficient for exact reconstruction if there is no undetected zone, otherwise, it is necessary to increase β to attain sufficient projection data. However, the assumption of north–south symmetry can significantly improve the situation. Such that β only has to be larger than 150 degrees for exact reconstruction. The *Cc* for the ART-TV and ART-TV-S methods show the same peak value of 0.97, indicating that the reconstructed images are comparable with sufficient projection data. For the same β at less than the peak value, the *Cc* is stronger for the ART-TV-S method. When using the same insufficient projection data, the ART-TV-S is generally more effective than the ART-TV method.

Figure 3 shows reconstructed images for the ART-TV and ART-TV-S methods from $\beta = 90^\circ$, 150° and 210°, with a gray scale window of [0, 3]. The ART-TV-S results are symmetrical about the *X*-axis because of the a priori knowledge of plasmaspheric north–south symmetry. For the ART-TV results, the northern portion is closer to the model than the southern portion. This is because the sampling positions are mainly in the northern region, while the southern portion has fewer opportunities to be detected due to blocking by the Earth.

The images with $\beta = 90^\circ$ correspond to small *Cc*. In this case, the quality of the images near the *X*-axis is much better than that near *Z*-axis. This is because the sampling trajectory is symmetrical about the *Z*-axis, lacking sampling data near the *X*-axis. The images near the *Z*-axis will be much better if the sampling trajectory is symmetrical about *X*-axis. This simulation is similar to the IMAGE mission which detected the plasmasphere from a high apogee above the North Pole, using sampling points mainly concentrated in the +*Z*-axis region and a projection angle β typically less than 90°. From the 2D images of $\beta = 90^\circ$, we can see that, even with the assumption of north–south symmetry, artifacts are inevitable. Despite this, the ART-TV-S method appears to provide a more accurate reconstructed image.

4. Conclusion and Discussions

In this study, we present the ART-TV-S method to reconstruct the plasmaspheric He^+ global density distribution from 2D EUV images. This method is an improved version of ART-TV with additional priori knowledge. In comparison with the ART-TV method, we find that the ART-TV-S method can effectively reconstruct images from imperfect projection data. In 2D simulations, the ART-TV-S method is shown to achieve exact reconstruction of an image with a projection angle of 150 degrees.

The ART-TV-S method can be extended to 3D reconstruction of EUV images, and we expect to apply this method to EUV images from IMAGE and the CE-3 spacecraft. Similar to the 2D case, the quality near the *X-Y* plane distant from the Earth is expected to be more accurate in 3D reconstructed images. By combining EUV images from IMAGE and CE-3, the reconstructed images will be significantly improved, especially near the *Z*-axis.

For the current study, the focus is to test and verify the new methods and the application of a uniform distribution has certain advantages for this purpose. With this simplification, it is easy to compare the reconstruction results from different methods and small differences between the results can be clearly recognized by adjusting the display window. In future work, we will use the ART-TV-S method to reconstruct a more realistic density model of the plasmasphere (e.g., Carpenter and Anderson, 1992; Ozhogin et al., 2012).

We should emphasize that the plasmasphere varies with magnetic activity, with our method being applicable to a "saturated" state (Sandel et al., 2007). During quiet periods, the plasmasphere can expand past $L = 7$ toward saturated configuration, which can be maintained until the plasmasphere begins to deplete as a result of increased magnetic activity. In addition, the actual noise in measurements (e.g. Poisson noise) can affect reconstructions. These problems are beyond the scope of the present paper, but in future work it may be worthwhile to consider the noise impact as well as reconstructions in different coordinates.

One important application of the ART-TV-S method is for reconstruction of the SXI from the SMILE mission (more information available at the website: https://sci.esa.int/web/smile). SMILE will perform SXI of large-scale structures in the magnetosphere, including the magnetosheath, magnetopause and cusps. The soft *X*-rays arise from the charge exchange interaction between solar wind heavy ions and Earth's neutral particles (Cravens, 2000). The measured value of the SXI imager is the line integration of volume emission that is proportional to the ion density (Cravens, 2000; Sun TR et al., 2015; Jorgensen et al., 2019). The imaging process of SXI is the same with as the projection process of CT, so the ART-TV method can be generalized to study SXI images from the SMILE mission. Moreover, a priori knowledge of north–south symmetry is reasonable for the magnetopause, since the cusp region is also north–south symmetric especially when the inter-planetary mag-

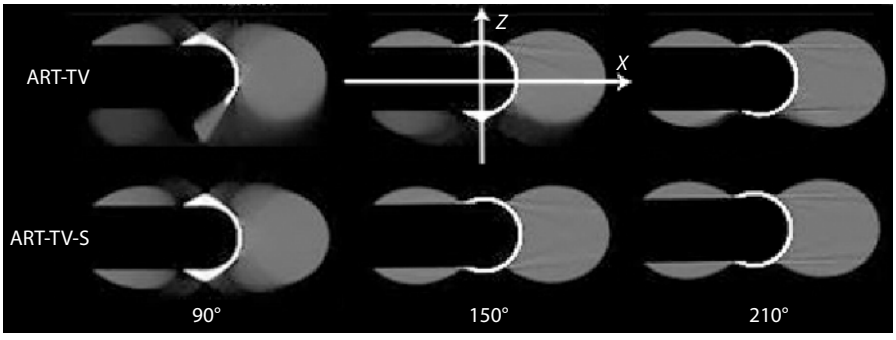

Figure 3. Images reconstructed by use of the ART-TV and ART-TV-S methods from different projection angles of 90°, 150° and 210°.

netic field component B_y is small. SMILE will perform scientific observations at an altitude of more than 50,000 km, so the projection angle can reach 83 degrees for a single orbit and 136–138 degrees for the three year life of the mission. From the results of this study, it is encouraging that we will be able to reconstruct SXI images from SMILE with the ART-TV-S method.

Acknowledgments

This work was supported by the National Natural Science Foundation of China (Grant Nos. 41904148, 41731070, 41874175), and in part by the Strategic Priority Program on Space Science, Chinese Academy of Sciences (Grant Nos. XDA15017000, XDA15350201, XDA15052500). Partial funding was provided by the Specialized Research Fund for State Key Laboratories of China. The authors would like to thank Tianran Sun and Xizheng Yu for providing the related information for the SMILE mission.

References

Carpenter, D. L., and Anderson, R. R. (1992). An ISEE/whistler model of equatorial electron density in the magnetosphere. *J. Geophys. Res.*, *97*(A2), 1097–1108. https://doi.org/10.1029/91JA01548

Craven, P. D., Gallagher, D. L., and Comfort, R. H. (1997). Relative concentration of He^+ in the inner magnetosphere as observed by the DE 1 retarding ion mass spectrometer. *J. Geophys. Res.*, *102*(A2), 2279–2289. https://doi.org/10.1029/96JA02176

Cravens, T. E. (2000). Heliospheric X-ray emission associated with charge transfer of the solar wind with interstellar neutrals. *Astrophys. J.*, *532*(2), L153–L156. https://doi.org/10.1086/312574

Cummings, W. D., O'Sullivan, R. J., and Coleman, P. J. Jr. (1969). Standing Alfvén waves in the magnetosphere. *J. Geophys. Res.*, *74*(3), 778–793. https://doi.org/10.1029/JA074i003p00778

He, F., Zhang, X. X., Chen, B., and Fok, M. C. (2011). Reconstruction of the plasmasphere from Moon-based EUV images. *J. Geophys. Res.*, *116*(A11), A11203. https://doi.org/10.1029/2010JA016364

He, H., Shen, C., Wang, H. N., Zhang, X. X., Chen, B., Yan, J., Zou, Y. L., Jorgensen, A. M., He, F., … Xu, R. L. (2016). Response of plasmaspheric configuration to substorms revealed by Chang'e 3. *Sci. Rep.*, *6*, 32362. https://doi.org/10.1038/srep32362

Herman, G. T. (1980). Image Reconstruction from Projection: the Fundamentals of Computerized Tomography. *Academic Press, New York*

Hsieh, J. (2009). *Computed Tomography: Principles, Design, Artifacts, and Recent Advances* (2nd ed). Bellingham: SPIE.

Huang, X. Q., Reinisch, B. W., Song, P., Green, J. L., and Gallagher, D. L. (2004). Developing an empirical density model of the plasmasphere using IMAGE/RPI observations. *Adv. Space Res*, *33*(6), 829–832. https://doi.org/10.1016/j.asr.2003.07.007

Huang, Y., Xu, R. L., Li, L., and Jin., X. (2009). Deduction of the global density of the plasmasphere reconstructed from the observation images using computed tomography technique-the earth's shelter. *Chin. J. Geophys.* (*in Chinese*), *52*(11), 2683–2688.

Huang, Y., Xu, R. L., Shen, C., Li, L., and Chen, Z. Q. (2012). Deduction of the global density of the plasmasphere reconstructed from the observation images using computer tomography technique -incomplete projection data. *Chin. J. Geophys.* (*in Chinese*), *55*(4), 1071–1077.

Huang, Y., Cheng, B. J., Liu., X. W., Shen, C., Zhang, Y. T., Li, L., and Zhang, L. Q. (2016). Reconstruction of Martian methane's spatial density distribution. *Chin. Sci. Bull.* (*in Chinese*), *61*(16), 1822–1827. https://doi.org/10.1360/N972015-01084

Huang, Y., Cheng, B. J., Liu., X. W., Shen, C., Zhang, Y. T., Li, L., and Zhang, L. Q. (2011). Deduction of the global density of plasmasphere reconstructed from the EUV images using CT method 2. Three dimensional parallel-beam ART reconstruction. *Chin. J. Geophys.* (*in Chinese*), *54*(7), 1691–1700. https://doi.org/10.3969/j.issn.0001-5733.2011.07.001

Jorgensen, A. M., Sun, T. R., Wang, C., Dai, L., Sembay, S., Zheng, J. H., and Yu, X. Z. (2019). Boundary detection in three dimensions with application to the SMILE mission: the effect of model-fitting noise. *J. Geophys. Res.*, *124*(6), 4341–4355. https://doi.org/10.1029/2018JA026124

Kim, E., Kim, Y. H., Jee, G., and Ssessanga, N. (2018). Reconstruction of plasmaspheric density distributions by applying a tomography technique to Jason-1 plasmaspheric TEC measurements. *Radio Sci.*, *53*(6), 866–873. https://doi.org/10.1029/2017RS006527

Li, C. F., Zhou, K. Y., Huang, D., Chen, Z. S., He, L., and Wang, Q. L. (2004). A knowledge-based automatic segmentation of the cerebral computerized tomography images. *Chin. J. Med. Instrum.* (*in Chinese*), *28*(3), 168–171. https://doi.org/10.3969/j.issn.1671-7104.2004.03.004

Li, C. L., Liu, J. J., Ren, X., Zou, W., Tan, X., Wen, W. B., Li. H., Mu., L. L., Su, Y., … Ouyang, Z. Y. (2015). The chang'e 3 mission overview. *Space Sci. Rev.*, *190*(1), 85–101. https://doi.org/10.1007/s11214-014-0134-7

Li, L., Kang, K. J., Chen, Z. Q., Zhang, L., Xing, Y. X., Yu, H. Y., and Wang, G. (2008). An alternative derivation and description of Smith's data sufficiency condition for exact cone-beam reconstruction. *J. X-Ray Sci. Technol.*, *16*(1), 43–49.

Li, L., Chen, Z. Q., Xu, R. L., Kang, K. J., Zhang, L., and Xing, Y. X. (2009). A study of the plasmasphere density distribution using computed tomography methods from the EUV radiation data. *Adv. Space Res.*, *43*(7), 1143–1147. https://doi.org/10.1016/j.asr.2008.10.013

Meier, R. R., Nicholas, A. C., Picone, J. M., Melendez-Alvira, D. J., Ganguli, G. I., Reynolds, M. A., and Roelof, E. C. (1998). Inversion of plasmaspheric EUV remote sensing data from the STP 72-1 satellite. *J. Geophys. Res.*, *103*(A8), 17505–17518. https://doi.org/10.1029/98JA01175

Nakamura, M., Yoshikawa, I., Yamazaki, A., Shiomi, K., Takizawa, Y., Hirahara, M., Yamashita, K., Saito, Y., and Miyake, W. (2000). Terrestrial plasmaspheric imaging by an extreme ultraviolet scanner on Planet-B. *Geophys. Res. Lett.*, *27*(2), 141–144. https://doi.org/10.1029/1999GL010732

Orr, D., and Matthew, J. A. D. (1971). The variation of geomagnetic micropulsation periods with latitude and the plasmapause. *Planet. Space Sci.*, *19*(8), 897–905. https://doi.org/10.1016/0032-0633(71)90141-3

Ozhogin, P., Tu, J., Song, P., and Reinisch, B. W. (2012). Field-aligned distribution of the plasmaspheric electron density: an empirical model derived from the IMAGE RPI measurements. *J. Geophys Res.*, *117*(A6), A06225. https://doi.org/10.1029/2011JA017330

Sandel, B. R., Broadfoot, A. L., Curtis, C. C., King, R. A., Stone, T. C., Hill, R. H., Chen, J., Siegmund, O. H. W., Raffanti, R., … Gallagher, D. L. (2000). The extreme ultraviolet imager investigation for the IMAGE mission. *Space Sci. Rev.*, *91*(1-2), 197–242. https://doi.org/10.1023/A:1005263510820

Sandel, B. R., and Denton, M. H. (2007). Global view of refilling of the plasmasphere. *Geophys. Res. Lett.*, *34*(17), L17102. https://doi.org/10.1029/2007GL030669

Sidky, E. Y., Kao, C. M., and Pan, X. C. (2006). Accurate image reconstruction from few-views and limited-angle data in divergent-beam CT. *J. X-Ray Sci. Technol.*, *14*(2), 119–139.

Sun, T. R., Wang, C., Wei, F., and Sembay, S. (2015). X-ray imaging of Kelvin-Helmholtz waves at the magnetopause. *J. Geophys. Res.*, *120*(1), 266–275. https://doi.org/10.1002/2014JA020497

Tuy, H. K. (1983). An inversion formula for cone-beam reconstruction. *SIAM J. Appl. Math.*, *43*(3), 546–552. https://doi.org/10.1137/0143035

Wang, C., and Branduardi-Raymond, G. (2018). Progress of Solar wind Magnetosphere Ionosphere Link Explorer (SMILE) mission. *Chin. J. Space Sci.*, *38*(5), 657–661. https://doi.org/10.11728/cjss2018.05.657